Surface & Coatings Technology 511 (2025) 132262

Contents lists available at ScienceDirect

Surface & Coatings Technology

journal homepage: www.elsevier.com/locate/surfcoat

Tuning the mechanical properties and toughness of TiAlN coatings deposited by low duty cycle pulsed magnetron sputtering from a rotating cylindrical target

Veronika Simova *, Oleg Zabeida, Luis Bernardo Varela, Jincheng Qian, Jolanta-Ewa Klemberg-Sapieha *, Ludvik Martinu

Department of Engineering Physics, Polytechnique Montréal, Montreal, Quebec H3T 1J4, Canada

ARTICLE INFO

Keywords:
Rotating cylindrical magnetron sputtering
Low duty cycle pulsed dc magnetron sputtering
TiAlN coatings
Residual stress
Nanoindentation toughness

ABSTRACT

Despite the promising capabilities, rotating cylindrical magnetron sputtering (CMS) has been relatively rarely described in the literature, especially regarding hard protective coating applications. In this study, we investigate the use of CMS in the pulsed dc mode with very low duty cycle (<10 %) to prepare model TiAlN coatings at relatively high deposition rates (4 μm/h). We examine the impact of key parameters, specifically, substrate bias and substrate temperature on the coating microstructure and properties. Particularly, we focus on the residual stress in the coatings and their nanoindentation toughness, as these characteristics are crucial for the understanding of the film behavior and optimizing coating architectures. TiAlN coatings prepared with a substrate bias of about −100 V exhibit dense morphology, and high hardness (28–30 GPa), while the level of compressive stress in the coatings can be significantly reduced by increasing substrate temperature (from −5.6 GPa to −2.3 GPa at room temperature and 400 °C, respectively). Furthermore, we show a linear relationship between the residual stress in the TiAlN coatings and their nanoindentation toughness (1.1 MPa·m$^{1/2}$ to 5.1 MPa·m$^{1/2}$). Our findings demonstrate that both substrate bias and temperature can be effectively used to control the microstructure, mechanical properties, toughness and compressive stress level in the coatings, thereby opening a possibility to mitigate loading stress in various applications.

1. Introduction

Magnetron sputtering (MS) is one of the most widely used physical vapor deposition (PVD) techniques for the fabrication of functional coatings for numerous applications [1–3]. However, to apply MS with standard planar magnetrons on a large scale, it is necessary to cope with various challenges such as low target utilization typically limited to 25–30 % [4,5] due to the non-uniform target erosion and formation of a stationary racetrack (i.e., erosion groove), which increases the costs. In addition, the presence of the racetrack results in process instabilities during reactive sputtering as discussed, e.g., in refs. [6–8]. Progressing target erosion during the deposition process results in changes in the effective magnetic field at the target surface, having a strong influence on the ionized fluxes and the deposition rate, and thus, significantly affecting the long-term process reproducibility [8]. In addition, in the reactive mode, the region outside the racetrack is completely covered by a dense compound layer (oxide or nitride), which can lead to arcing [9].

In contrast, cylindrical magnetron sputtering (CMS) using a rotating cylindrical target, differs from traditional methods in that the racetrack is not stationary, but moves across the target surface. This results in uniform erosion and prevents formation of an erosion groove, leading to a significantly higher effective target utilization [10]. The large material inventory also results in a longer useful time and decreased costs [5,11]. Another important advantage of rotating cylindrical targets is the fact that only a portion of the target is exposed to the plasma for a short time, which enhances target cooling compared to standard planar magnetrons. This makes it possible to apply higher powers to the magnetron and to achieve higher deposition rates [10]. Moreover, the growth of non-stable compounds on the target surface can be strongly reduced due to continuous plasma cleaning during the target rotation, minimizing arcing probability in the reactive sputtering mode [12,13]. The main drawbacks, however, include the complexity of the system design and a limited supply of available target materials [5].

Due to its many benefits, CMS has been explored for industrial

* Corresponding authors.
E-mail addresses: veronika.simova@polymtl.ca (V. Simova), jolanta-ewa.sapieha@polymtl.ca (J.-E. Klemberg-Sapieha).

https://doi.org/10.1016/j.surfcoat.2025.132262
Received 7 May 2025; Received in revised form 8 May 2025; Accepted 9 May 2025
Available online 10 May 2025
0257-8972/© 2025 The Authors. Published by Elsevier B.V. This is an open access article under the CC BY license (http://creativecommons.org/licenses/by/4.0/).

production of large-area in-line optical coatings [11,14–16]. Furthermore, CMS provides valuable opportunities for research to investigate certain fundamental effects in sputtering processes (e.g., the effect of redeposition described in [17,18]) which would not have been observed with planar magnetrons.

CMS appears to be very well adapted for low duty cycle magnetron sputtering techniques (pulsed dc, HiPIMS) and to cope with the otherwise reduced deposition rate in these regimes, which limits their full implementation in industry for the fabrication of high-quality protective coatings, especially in HiPIMS mode. Such an approach benefits from a large ratio between the target and substrate surface, providing an enhanced deposition rate and ion flux, while increasing the target utilization. Nevertheless, the use of CMS for the preparation of protective coatings is still largely unexplored or unpublished. Inspired by recent research activities on HiPIMS, which has been proven to generate a dense plasma with a high degree of ionization of the sputtered atoms, making it possible to deposit high-quality smooth coatings even on complex-shaped substrates (as shown, e.g., in refs. [19–21]), in this work we investigate the use of low duty cycle pulsed dc magnetron sputtering (LDMS), previously described, e.g., in [22,23], in conjunction with CMS for the preparation of hard protective coatings. Specifically, TiAlN with a Ti/Al stoichiometric ratio of 1 has been selected here as a model material widely used in aerospace and manufacturing applications, particularly due to the combination of high hardness, wear resistance, thermal stability and oxidation resistance [24–28]. We describe the deposition process and the cylindrical magnetron discharge characteristics, while discussing the effect of substrate bias and/or substrate heating on the composition, microstructure, and properties, including the nanoindentation toughness, of TiAlN coatings. Particularly, we study the development of residual stress (RS) in the coatings, as RS plays an important role in the performance of the protective coatings in real-life applications.

2. Experimental details

2.1. Coating preparation

The TiAlN coatings were prepared in a vacuum deposition system consisting of a 700 l volume rectangular stainless steel chamber equipped with a rotatable cylindrical magnetron (Sputtering Components Inc., CM125 TRM-Bar™) and a stationary substrate holder (see a schematic illustration in Fig. 1). The chamber was evacuated by a turbomolecular pump backed by a rotary roughing pump. The base pressure in the chamber prior to experiments was below 2×10^{-6} Torr (measured by a Pirani gauge). In order to remove surface contamination, the substrates were sputter cleaned in a pulsed dc discharge (Advanced Energy, Pinnacle Plus) for 30 min at a constant Ar pressure of 15 mTorr and a substrate bias voltage of −500 V.

The coatings were deposited onto p-type Si(100) substrates using an alloy TiAl cylindrical target (robeko GmbH & Co. KG) rotating at a speed of 10 rpm, total length of 550 mm, outer diameter of 152 mm with a Ti:Al ratio of 50:50 in Ar + N_2 gas mixtures. The flow of Ar was kept fixed at 57 sccm, while the N_2 flow was varied from 0 sccm up to 20 sccm, resulting in the total pressure in the range of 3–3.5 mTorr (measured by a capacitance diaphragm gauge). LDMS pulses were produced using a pulse generator (Magpuls Stromversorgungs Systeme GmbH, MP-2-HC) powered by an external dc power supply (Rübig GmbH & Co KG, MP 120). Typical deposition and pulsing parameters are listed in Table 1.

The substrate-to-target distance was kept constant at 85 mm. The substrates were held at a floating potential or intentionally biased using a dc power supply (Advanced Energy, Pinnacle Plus). Their temperature was maintained at a preset temperature between RT and 400 °C.

An optical emission spectrometry (OES) system (PLASUS GmbH, EMICON SA) was connected to the sputtering system for in-situ real-time monitoring of the voltage and current waveforms, plasma emission spectra and evolution of selected emission lines during the deposition process.

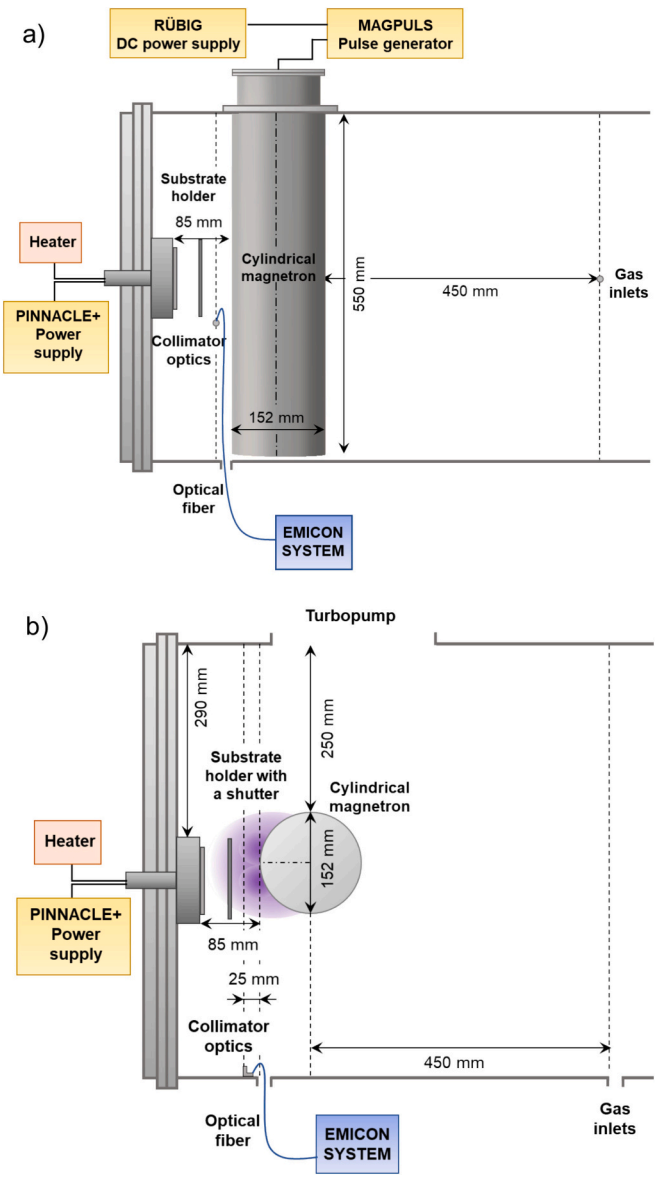

Fig. 1. Schematic illustration of the deposition system with the rotating cylindrical magnetron: a) top view, b) side view.

2.2. Coating characterization

The coating microstructure was investigated by X-ray diffraction (XRD). The measurements were carried out in the θ-2θ mode from 20° to 90° on a Bruker D8-Discover diffractometer using CuKα radiation (40 kV, $\lambda = 0.154$ nm). The diffraction patterns were evaluated using the PDF-4+ database and DIFFRAC.EVA software package from Bruker.

Scanning electron microscopy (SEM) observations were performed using a field emission gun JEOL JSM7600F system operating at 10.0 kV. The chemical composition of the coatings was determined by energy dispersive X-Ray spectroscopy (EDS) carried out using an EDS X-MaxN detector from Oxford Instruments. Despite EDS is generally considered to be less effective for detection of light elements, we consider it to be appropriate for the evaluation of the chemical composition of TiAlN coatings based on our recent study showing very good agreement between different characterization methods (EDS, ERD-TOF and XPS) even for light elements like B and C [29].

Surface roughness values, S_a, of the coatings were assessed by 3D

Table 1
Process parameters used for the deposition of the TiAlN coatings from the rotating cylindrical magnetron. Discharge parameters were determined from the waveforms (see Fig. 2).

	LDMS	Pulsed dc
Total pressure	3.4 mTorr	
N_2 partial pressure	0.4 mTorr	
Ar flow rate	47 sccm	
N_2 flow rate	15 sccm	
Pulse length	100 μs	1000 μs
Frequency	0.91 kHz	0.91 kHz
Duty cycle	9.1 %	91 %
Magnetron voltage	−740 V	−450 V
Pulse current	23 A	3.9 A
Pulse current density (target)	0.12 A/cm^2	0.02 A/cm^2
Peak current	33 A	10 A
Peak current density	0.17 A/cm^2	0.05 A/cm^2
Pulse power	17.6 kW	1.8 kW
Pulse power density	88 W/cm^2	9 W/cm^2
Peak power	24.4 kW	4.5 kW
Peak power density	122 W/cm^2	22.5 W/cm^2
Average power	1.6 kW	
Average power density	8 W/cm^2	
CM rotation speed	10 rpm	
Substrate bias voltage	Floating or −100 V	
Substrate temperature	RT up to 400 °C	

optical profilometry performed with a Bruker ContourX-100 profilometer.

Mechanical properties (hardness, H, and reduced Young's modulus, E_r) were investigated by nanoindentation using a Bruker Hysitron TI 950 Triboindenter equipped with a Berkovich diamond pyramidal tip. Each coating was probed by a 4 × 4 indentation matrix. For each indentation of the matrix, a multicycle load ranging from 2 to 200 mN was used. The load-displacement curves were analyzed using the Oliver and Pharr methodology [30].

The coating toughness, K_c, was evaluated through nanoindentation with a cube-corner tip, and calculated using the following equation [31]:

$$K_c = \alpha \cdot \sqrt{\frac{E}{H}} \cdot \frac{F}{c^{\frac{3}{2}}}, \quad (1)$$

where α is an empirical calibration constant related to the geometry of the indenter (0.033 for a cube-corner indentation tip [32]), E and H are elastic modulus and hardness, respectively, F is the applied load, and c is the length of the radial cracks from the center of the indent. To create radial cracks for evaluation of the nanoindentation toughness, a matrix of 7 × 7 indents with a load ranging from 10 to 500 mN was used. Subsequently, the length of the cracks created during nanoindentation was measured by SEM.

The residual stress, σ, and stress-free lattice parameters, a_0, were evaluated by multi-hkl grazing incidence XRD (MGIXRD) measurements taken at different angles of incidence to scan all the coating thickness. The methodology has been described in detail elsewhere [33]. The X-ray elastic constants (XECs), $\frac{1}{2}S_2^{hkl}$ and S_1^{hkl}, were obtained from the elastic stiffness constants for TiAlN ($C_{11} = 447$, $C_{12} = 158$, $C_{44} = 203$) using the Kroner model via the IsoDEC software [34].

The crystallite size was calculated using the Scherrer's formula:

$$d_{avg} = \frac{k \cdot \lambda}{\beta \cdot cos\theta} \quad (2)$$

where k is the crystallite shape factor (approx. 0.9), λ is the X-ray wavelength (0.154 nm), β is the full width at half maximum (FWHM) of the diffraction peak (in radians), and θ is the Bragg's angle (in degrees).

3. Results and discussion

In this section, we discuss the results for TiAlN coatings prepared by rotating-target CMS in the LDMS mode. First, we present the deposition parameters and discharge characteristics (Section 3.1). Then, we compare the deposition rates achieved in LDMS and conventional pulsed dc modes, as well as when using cylindrical or planar magnetrons (Section 3.2). Thereafter, we discuss the composition, and microstructure (Section 3.3), mechanical properties (Section 3.4), residual stress (Section 3.5), and nanoindentation toughness (Section 3.6) of the TiAlN coatings prepared by rotating CMS in the LDMS mode at various substrate temperatures (up to 400 °C) and at a floating potential, or when using substrate bias.

3.1. Discharge characteristics

Process parameters used for the deposition of the TiAlN coatings are listed in Table 1, and typical time evolution of the magnetron voltage and discharge current for depositions in the LDMS mode is shown in Fig. 2. At the end of the rectangular negative voltage pulse of −740 V, a high positive voltage overshoot of +302 V, accompanied by negative values of the discharge current of −4 A, can be observed. In fact, such voltage reversal (positive kick) is beneficial for the coating deposition, since it leads to a bombardment of the growing films by ions with a high kinetic energy for a very short time, and thus to film densification without using any additional substrate bias [35–37]. The current waveform exhibits a triangular-like shape, which might be attributed to a discharge mode being dominated by working gas recycling, where the conditions for effects like gas rarefaction and self-sputtering have not been completely established [38,39].

For comparison, parameters for pulsed dc depositions with high duty cycle (at the same average power as in LDMS), are also shown in Table 1. In the conventional pulsed dc mode, the pulse and peak currents were much lower (approx. 4 A and 10 A, respectively) compared to LDMS, as well as the positive voltage overshoots (tens of V only).

Typical spectra recorded by OES during the deposition of TiAlN coatings in LDMS and conventional pulsed dc modes are presented in

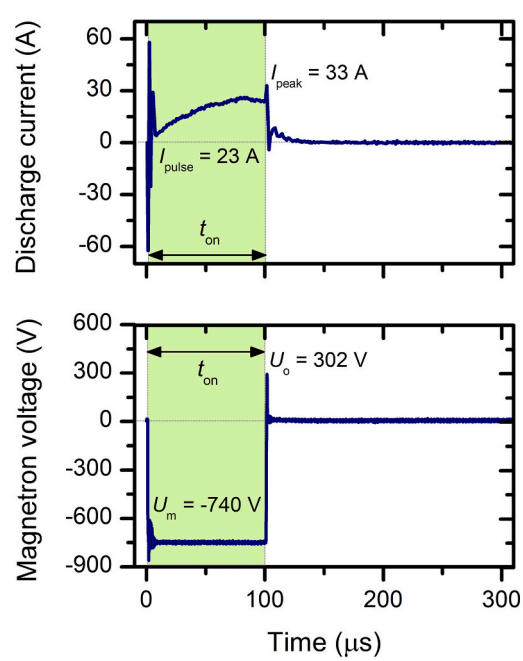

Fig. 2. Time evolution of the magnetron voltage and the discharge current during rotating cylindrical LDMS deposition of TiAlN coatings in an Ar + N_2 gas mixture, at a voltage pulse length of 100 μs, frequency of 0.91 kHz, and a rotation speed of 10 rpm.

Fig. 3a and b, including an indication of the emission lines selected for real-time monitoring during the process. Fig. 3a is a representative example of an optical spectrum characteristic for low duty cycle discharges as it is dominated by metallic species (Al, Ti, Ti^+), while the intensity corresponding to process gas (Ar, N_2, N_2^+) is relatively low, which can be also typically observed in HiPIMS. On the other hand, in conventional pulsed dc discharges (see Fig. 3b), the emission intensity of metallic species is much lower compared to the intensity of Ar.

3.2. Deposition rate

As already mentioned, one of the main drawbacks of low duty cycle magnetron sputtering is its relatively low deposition rate. Thus, we prepared two sets of TiAlN coatings by LDMS and conventional pulsed dc magnetron sputtering to compare the deposition rates in the CMS configuration (see Fig. 4a and b). In the metallic regime (0 sccm of N_2), the deposition rate is 4.6 μm/h and 7 μm/h in the LDMS and pulsed dc modes, respectively, which represents a drop in the deposition rate by 35 % in LDMS compared to the pulsed dc mode. The N_2 admixture (up to 20 sccm) resulted in a reduction in the deposition rate by additional 35 % in the pulsed dc discharges, while it dropped by only 20 % in LDMS. Consequently, the difference in the deposition rate between the conventional pulsed dc and LDMS is much smaller in the reactive regime than in the metallic regime. Note also that the pulse power in the LDMS mode increased by approximately 115 % in the reactive regime, but only by 25 % in the pulsed dc regime. This behavior might be related to effects such as different levels of poisoning and reactive gas gettering in different pulsing modes.

One of our goals in this work has been to prove if using CMS in the LDMS mode could enhance the deposition rate, which is generally significantly reduced in low duty cycle magnetron sputtering techniques. In Table 2 and Fig. 4, we show deposition rates of TiAlN coatings obtained in LDMS with cylindrical magnetron in the present work compared to the values reported in the literature for planar magnetrons. Since such comparison is not straightforward and depends on many factors (e.g., power density and target racetrack area, substrate-target distance, pressure, gas mixture composition, etc.), we selected examples of $Ti_{1-x}Al_xN$ coatings with a similar composition (close to $x = 0.5$) deposited in modes similar to LDMS used here from a single TiAl alloy target. For example, in our previous work on TiAlN coatings produced by HiPIMS from a planar magnetron [40], the deposition rate was almost 9× lower despite only a slightly reduced average power density.

It should be noted here that we considered the area of the racetrack (based on the measured distribution of the magnetic field on the target surface) to calculate the power density, while it can also be frequently calculated based on the target area. In addition, using a cylindrical target benefits from a large ratio between the surface of the target and substrate, increasing the number of metallic species arriving to the substrate from different directions, which can also lead to an apparent increase in the deposition rate.

3.3. Composition and microstructure

Figs. 5 and 6 show the chemical composition and stoichiometry of the TiAlN coatings prepared at different substrate temperatures with or without bias. Note that in all TiAlN coatings, we found a slightly higher content of Al compared to Ti, i.e., $x = Al/(Ti + Al) > 0.5$, even though the declared target composition is Ti:Al = 50:50 at.%. The coating composition is a result of an interplay of complex processes that occur not only during sputtering from an alloy target (e.g., difference in sputtering yields for Ti and Al [44], reactivities with N [45] or emission angles [46]), but also during the transport of sputtered particles in the plasma (scattering) or on the surface of the growing films (different sticking coefficients), and thus, the composition of the coatings does not

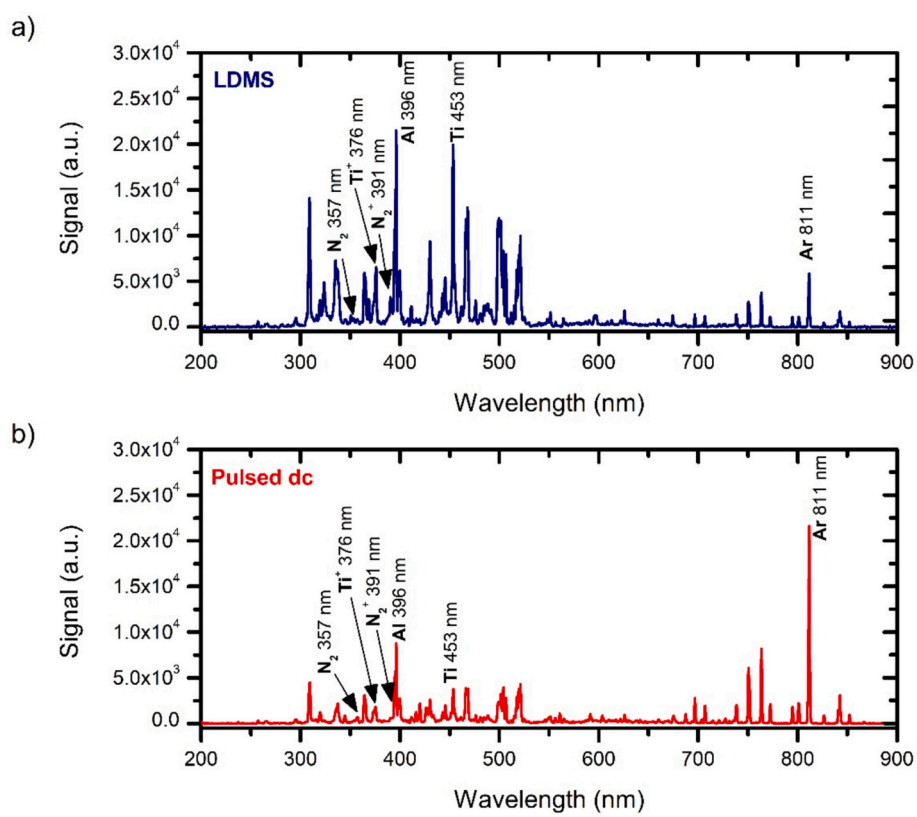

Fig. 3. Typical optical emission spectra for a) LDMS and b) conventional pulsed dc discharges during the deposition of TiAlN coatings from the rotating cylindrical magnetron with indicated lines selected for real-time plasma monitoring.

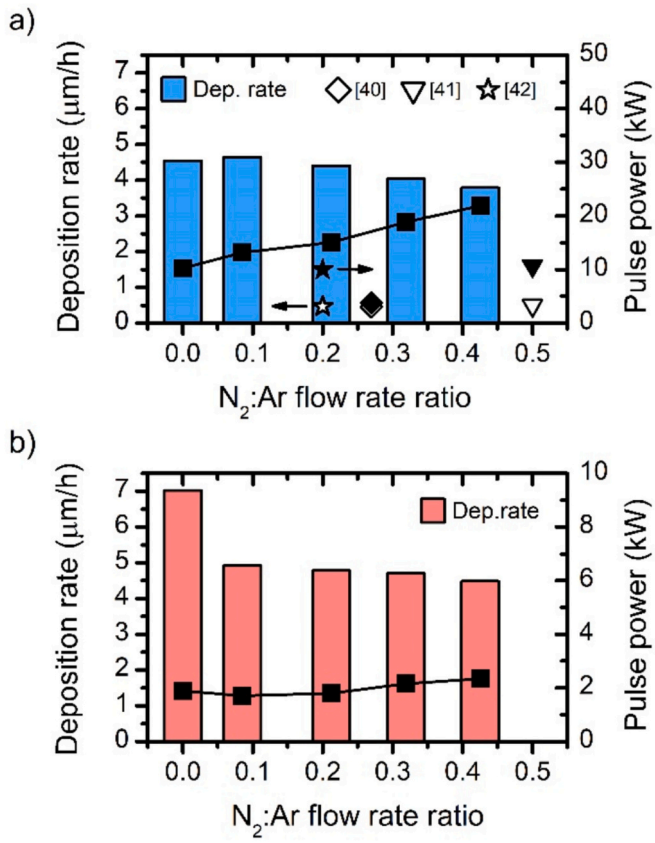

Fig. 4. Comparison of the deposition rates and pulse powers at various N_2 flow rates during deposition of the TiAlN coatings from the rotating cylindrical target in a) LDMS and b) conventional pulsed dc modes. For comparison, data from [40–42] are shown (empty symbols – deposition rate, full symbols – pulse power).

necessarily have to correspond to the target composition (as also investigated, e.g., in [47]).

The ratio between the Al and Ti contents is slightly reduced when the substrate bias is used at room temperature (see Fig. 6) which can be caused by: (i) preferential re-sputtering of Al (as also observed, e.g., in [41,48]); (ii) a higher degree of ionization of Ti particles and preferential attraction of Ti^+ ions to the negatively biased substrates [48]; and (iii) an increasing effect of back scattering of lighter Al species from the substrate [24,49,50]. In addition, as can be seen in Figs. 5 and 6, the concentration of N in the TiAlN coatings slightly increased with substrate biasing.

Fig. 7 compares the microstructures of TiAlN coatings prepared at different substrate temperatures and at a floating potential (U_{fl}) or when a substrate bias was used (U_s). Positions of all peaks in the XRD patterns have been found between the standard positions of c-TiN (JCPDS card 38-1420) and c-AlN (JCPDS card 25-1495), indicating a (Ti, Al)N solid solution with a mixture of (111), (200), (220), (311) and (222) orientations.

For the maximum substrate temperature used (400 °C), a presence of new features on the right shoulders of the (111) and (220) peaks can be observed at 2θ values of 38.81° and 64.76°, respectively. These peaks can be most probably assigned to h-AlN (JCPDS card 00-008-0262). When the substrate bias is used at high temperatures, no distinct peaks related to a formation of new Al-containing phases could be identified but note an apparent asymmetry of the (111) and (220) peaks.

The resulting texture is generally determined by a competition between the thermodynamic driving forces (surface energy and strain energy) and kinetic aspects to minimize the total energy of the system during the film growth [51–53]. TiAlN coating deposited at a floating substrate potential and room temperature, i.e., under low ion-

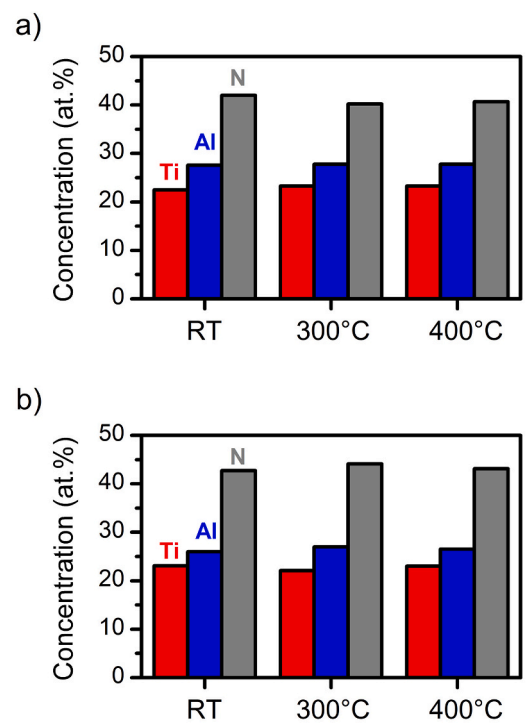

Fig. 5. Chemical composition of TiAlN coatings prepared by rotating cylindrical LDMS at various substrate temperatures and at a) a floating potential, or b) using a substrate bias of about −100 V.

Table 2
Comparison of the deposition rates achieved for TiAlN coatings produced by low duty cycle magnetron sputtering techniques (LDMS or HiPIMS) using cylindrical or planar magnetrons.

Coating (at. %)	Target (at.%)	Dep. rate (μm/h)	Substrate-target distance (mm)	Pressure (mTorr)	Duty cycle (%)	Avg. power (kW)	Avg. power density (W/cm^2)	Ref.
$Ti_{45}Al_{55}N$	Cylindr. $Ti_{50}Al_{50}$	4.0	85	3.4	9.1	1.6	8.0	This work
$Ti_{42}Al_{58}N$	Planar $Ti_{50}Al_{50}$	0.46	100	3	8	0.3	6.6	[40]
$Ti_{59}Al_{41}N$	Planar $Ti_{67}Al_{33}$ (wt %)	0.50	110	5	7.5	0.8	–	[41]
$Ti_{47}Al_{53}N$	Planar $Ti_{60}Al_{40}$	0.47	110	3	10	1	5.5	[42]
$Ti_xAl_{1-x}N$	Planar $Ti_{50}Al_{50}$	1.0–2.2	55–145	1.5–7.5	8	15	19.2	[43]

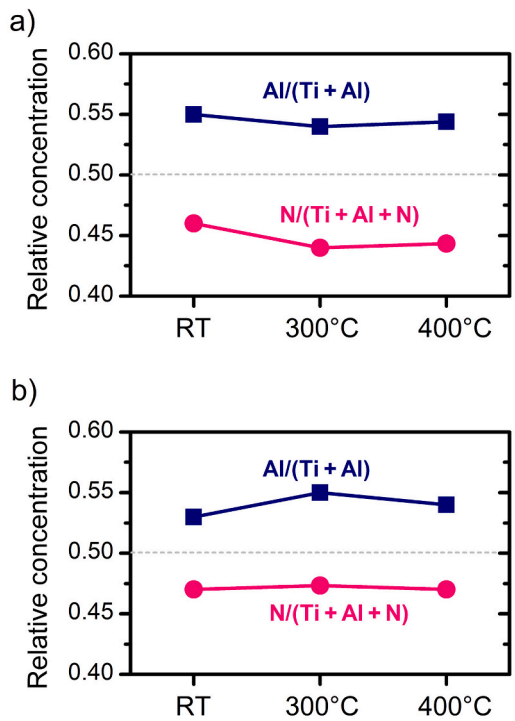

Fig. 6. Stoichiometry of TiAlN coatings prepared by rotating cylindrical LDMS at various substrate temperatures and at a) a floating potential, or b) using a substrate bias of about −100 V.

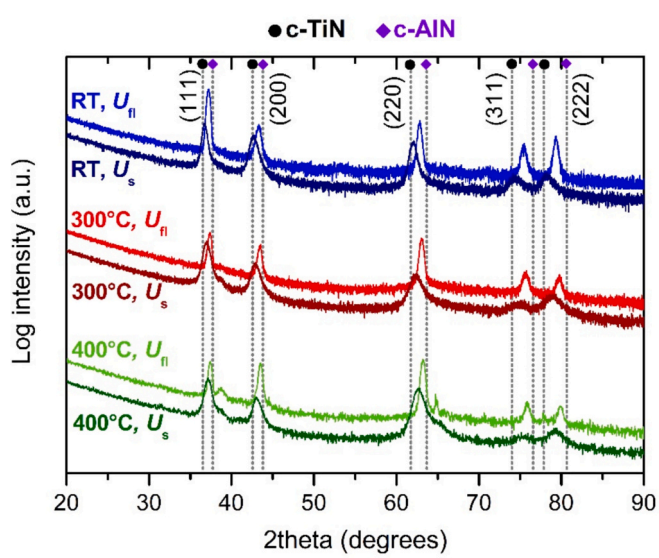

Fig. 7. Microstructure evolution of TiAlN coatings prepared by rotating cylindrical LDMS at various substrate temperatures and at a floating potential, or using a substrate bias of about −100 V.

bombardment conditions, develops a dominant (111) preferred orientation. This is typical for TiN and TiAlN coatings crystallizing in face-centered cubic B1 NaCl-type structures, where [111] represents the fastest growing directions. Under conditions approaching thermodynamic equilibrium (when the surface energy is the dominant contribution to the total energy), such as at high temperatures, the growth of (200) and (220) orientations is favored due to their lower surface energy in the B1 NaCl-type structures [54]. Under enhanced ion bombardment during substrate biasing, increased flux of N_2^+ ions attracted to the substrate, subsequently collisionally dissociated when impinging the substrate, and consequently increased N coverage significantly reduce Ti adatom mobility on (200) oriented grains, causing the transition from (111) to (200) orientation [55]. In addition, (111) orientation with the highest density of atoms is most sensitive to collision cascades and possible re-sputtering, and thus, (200) and (220) planes, more open for ion channelling [52,53,56], are preferred under ion bombardment.

Besides the changing crystal orientation, we can also observe a slight peak shift to different 2θ angles depending on the substrate temperature and bias. Generally, the peak shift can be related to a change in the composition (shown in Figs. 5 and 6) due to different atomic radii of individual elements incorporated in the coatings, which results in changing interplanar distances and hence a shift of diffraction peaks to different 2θ values [41]. In addition, the peak shift can also be an indication of changing residual stress in the coatings, which will be discussed further in Section 3.5. With substrate heating, the diffraction peaks appear at slightly higher 2θ angles, indicating a reduced compressive stress compared to the TiAlN coatings prepared at room temperature. On the contrary, substrate bias shifts the diffraction peaks to lower angles, which might be a sign of an increasing compressive stress in the TiAlN coatings. Moreover, an obvious peak broadening when substrate bias is used can be an indication of grain refinement due to increased energy of ion bombardment.

To distinguish between the contributions of the chemical composition or the residual stress, Fig. 8 shows a comparison of the stress-free lattice parameters calculated for the TiAlN coatings with lattice parameters as expected for the respective coating composition determined from the Vegard-like dependence [57].

It can be seen that the stress-free lattice parameters a_0 increase with substrate bias, from 0.419 to 0.424 at room temperature which can be explained by: (i) decreased Al content in the c-(Ti, Al)N phase; or (ii) increased generation of defects during ion bombardment.

Based on the Vegard-like dependence, the high a_0 values of the TiAlN coatings corresponding to high values of [Ti]/([Ti] + [Al]) ratios (0.62 and 0.98), suggest that the c-(Ti, Al)N phase contains less Al than expected, which must be compensated by formation of Al-rich phases [57,58]. However, no presence of such Al-rich phases could be detected by XRD for the TiAlN coatings prepared at room temperature (see Fig. 7). In addition, despite slightly reduced Al content in the coatings could be detected by EDS (Fig. 6) when substrate bias was used ([Ti]/([Ti] + [Al]) increased from 0.45 to 0.47), this could not explain such a significant increase in a_0 values shown in Fig. 8. In addition, in the case

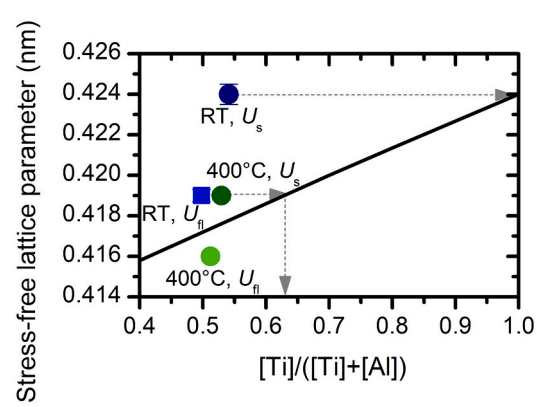

Fig. 8. Comparison of the stress-free lattice parameters determined for TiAlN coatings prepared by rotating cylindrical LDMS at various substrate temperatures and at a floating potential (squares), or using a substrate bias of about −100 V (circles) with the Vegard-like dependence (solid line). According to the Vegard-like dependence, the lattice parameters of 0.419 nm (RT, U_{fl}), 0.424 nm (RT, U_s), 0.416 nm (400 °C, U_{fl}), and 0.419 nm (400 °C, U_s) correspond to [Ti]/([Ti] + [Al]) of 0.62, 0.98, 0.40 and 0.62 in c-Ti−Al−N, respectively.

of the TiAlN coating prepared with substrate bias, the Vegard-like dependence suggests almost complete segregation of the material in TiN and AlN, which is very unlikely, since the XRD diffractograms in Fig. 7 clearly show c-(Ti, Al)N structure. Thus, we can conclude that the dominant contribution comes from higher amount of stress-generating defects due to ion bombardment, as also shown, e.g. in [33,59].

At high temperatures (400 °C), the a_0 values decrease compared to the coatings prepared at room temperature. When no substrate bias was used, it is even lower than the lattice parameter predicted by the Vegard-like dependence. This might be related to slightly reduced N content in the coatings prepared at high temperatures (see Fig. 6a). Missing N in the c-(Ti, Al)N phase leads to a shrinkage and deformation of the lattice structure and consequently decrease in the stress-free lattice parameter [60].

Fig. 9 presents cross-sections and surface SEM images of the TiAlN coatings prepared at different substrate temperatures and bias conditions. All coatings possess a columnar microstructure with all columns oriented in the direction perpendicular to the substrate. The coatings produced with no bias (Fig. 9a–c and g–i) exhibit a more open morphology consisting of pyramidal columns with rough conical tops, resulting in a higher surface roughness ($S_a \approx 30$ nm). Ion bombardment under bias conditions (shown in Fig. 9d–f and j–l) gives rise to densification of the coatings which then possess a more compact microstructure with finer grains and a smoother surface ($S_a < 3$ nm).

Due to a reduced current (and hence reduced power) during depositions (controlled by the voltage) with substrate heating, we also observe a lower thickness of the coatings prepared at 300 °C and 400 °C. Further reduction in the coating thickness by approximately 12 % when the substrate bias was used is related to enhanced mobility of the adatoms induced by the combination of high temperatures and ion bombardment, leading to the migration of small grains to the boundaries, reduction in vacant sites, and overall coating densification

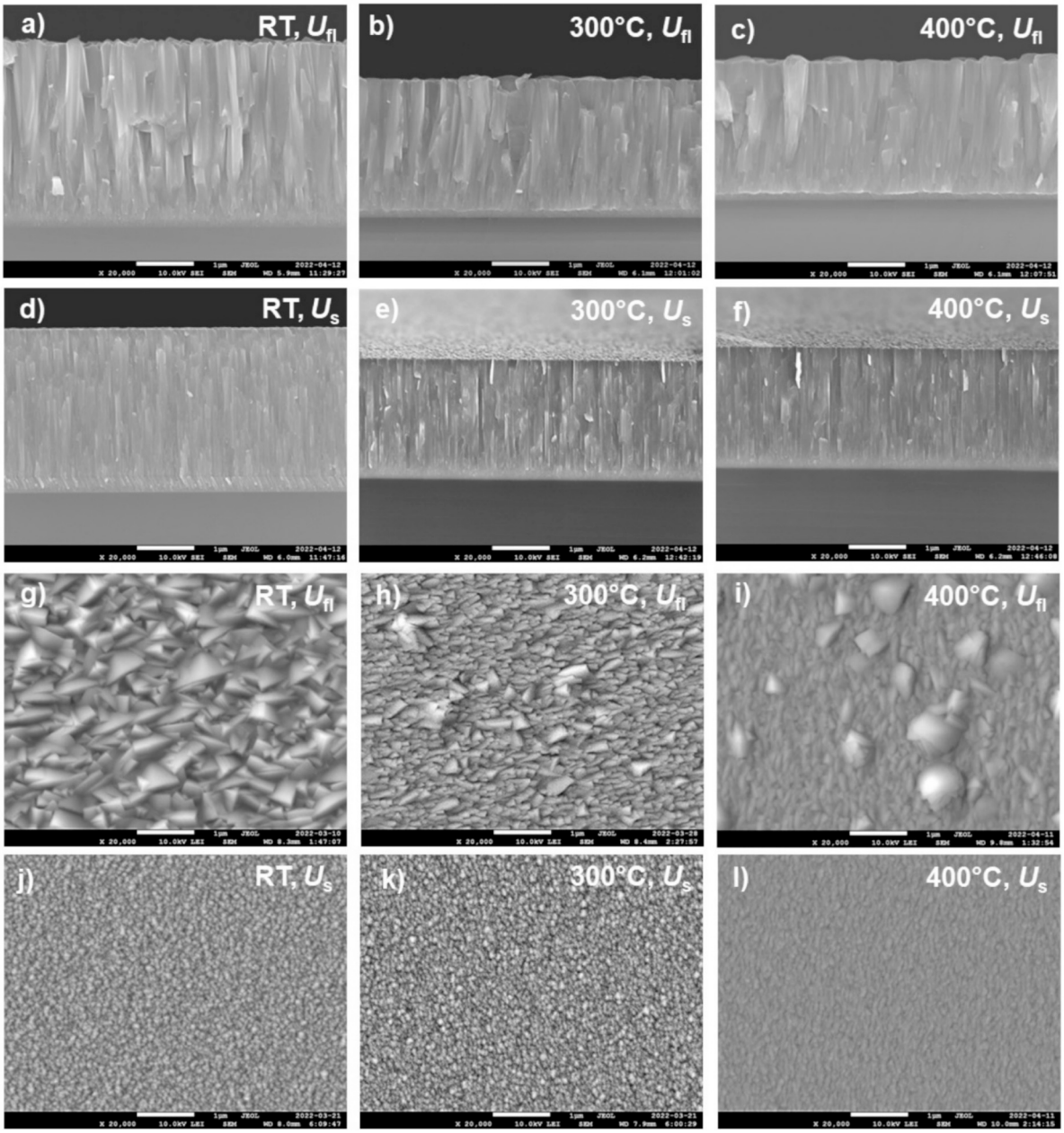

Fig. 9. Cross-section (a–f) and top-view (g–l) SEM micrographs of TiAlN coatings prepared by rotating cylindrical LDMS at various substrate temperatures, and at a floating potential or using a substrate bias as indicated on the micrographs.

[61,62].

3.4. Mechanical properties

Fig. 10a and b shows the hardness and reduced Young's modulus of TiAlN coatings prepared at different substrate temperatures and substrate bias. The substrate heating itself (at a floating potential) results in an enhancement of mechanical properties (Fig. 10a). However, the impact of the substrate heating is less significant compared to the effect of substrate bias, as the hardness increases only up to 25 GPa compared to 30 GPa achieved with substrate biasing at room temperature (see Fig. 10b). All TiAlN coatings prepared with substrate bias and at different temperatures possess relatively high hardness in the range between 28 GPa and 30 GPa.

The evolution of the mechanical properties can be attributed to several effects: (i) change in the texture (see Fig. 7), namely decreasing the intensity of the (111) orientation which is the preferred orientation for sliding [63]; (ii) grain refinement, as described by the well-known Hall-Petch equation [64,65]; and (iii) residual stress – it is generally believed that high compressive stress leads to a higher hardness [66,67].

In addition, it is known that the substrate bias affects the mobility of metallic atoms during the coating deposition. This can result in a nonuniform local distribution of Ti and Al in the coatings, as reported in [57]. Although such micro-segregation is hardly detectable by XRD, it can contribute to the formation of local microstrains and consequently, to an enhancement in hardness. Note the apparent differences in the expected [Ti]/([Ti] + [Al]) ratios based on the Vegard dependence (Fig. 8) and as determined by EDS (Fig. 6), suggesting that a presence of low amounts of Ti-rich or Al-rich phases not detected by XRD is possible.

Fig. 10c and d shows the H/E_r and H^3/E^2 ratios which have frequently been reported to control the elastic strain to failure and resistance to plastic deformation, respectively [68], and can be considered as indicators of fracture toughness (will be further discussed in Section 3.6) [69], tribological behavior [70], or erosion performance [68]. As can be seen, the substrate bias results in significantly increased both H/E_r and H^3/E^2 ratios, which can be mainly related to the enhancement of hardness shown. Therefore, in the case of the TiAlN coatings produced with substrate biasing, enhanced toughness, and hence improved tribological and erosion performance, can be expected.

3.5. Residual stress and grain size

In the previous part (Section 3.4), we mentioned that one of the main effects on the mechanical properties arises from the residual stress; this is now demonstrated Fig. 11 together with the average grain size. At all substrate temperatures and with no substrate bias (floating potential), the average residual stress in the TiAlN coatings is compressive and low, approximately −1 GPa, and the average crystallite size is in the range of 15–20 nm.

Substrate biasing leads to a substantial increase in the compressive stress up to −5.6 GPa (corresponding to the maximum hardness of 30 GPa in Fig. 10b) at room temperature, and also to a grain refinement (average grain size of approximately 9 nm). This reduction in the crystallite size can be related to the incorporation of inert gas atoms and an increasing number of surface defects generated by the ion bombardment giving rise to an increased number of preferential nucleation sites [71], but also limiting the migration of grain boundaries [72]. Consequently, smaller grains are formed during the film growth. With increasing substrate temperature, the compressive stress in the coatings is significantly reduced (−2.3 GPa), while the average crystallite size remains stable.

These results suggest that it is possible to prepare TiAlN coatings with a high hardness at levels of residual stress optimized for specific applications.

3.6. Nanoindentation toughness

SEM images of cracks induced by nanoindentation and used for the calculation of nanoindentation toughness of the TiAlN coatings are presented in Fig. 12. As can be seen in Fig. 12c, in the case of TiAlN coating produced at 400 °C and no bias, the generated cracks were not along the radial directions, and therefore, it was not possible to calculate the nanoindentation toughness for this sample.

The resulting nanoindentation toughness of the TiAlN coatings is presented in Fig. 13 as a function of compressive stress. This dependence can be well fitted by a straight line indicated in the graph, and thus, the

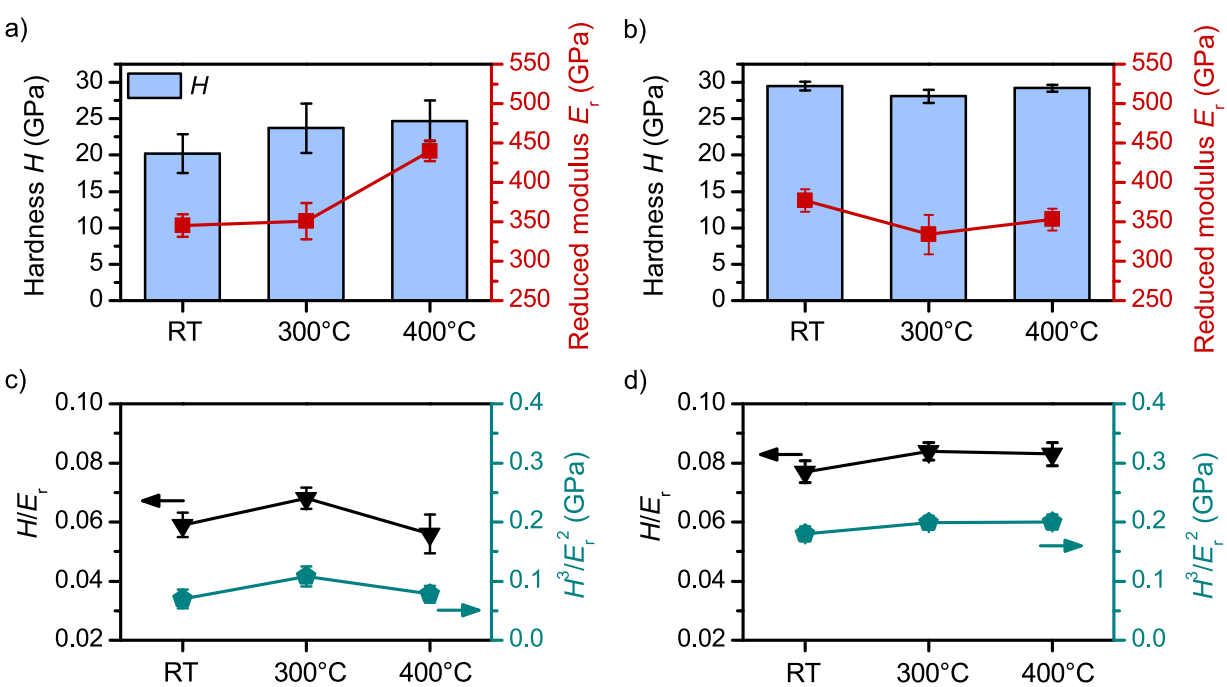

Fig. 10. Mechanical properties (hardness, H, and reduced Young's modulus, E_r) and H/E_r and H^3/E^2 ratios of TiAlN coatings prepared by rotating cylindrical LDMS at various substrate temperatures and at a floating potential (a, c), or when using a substrate bias of about −100 V (b, d).

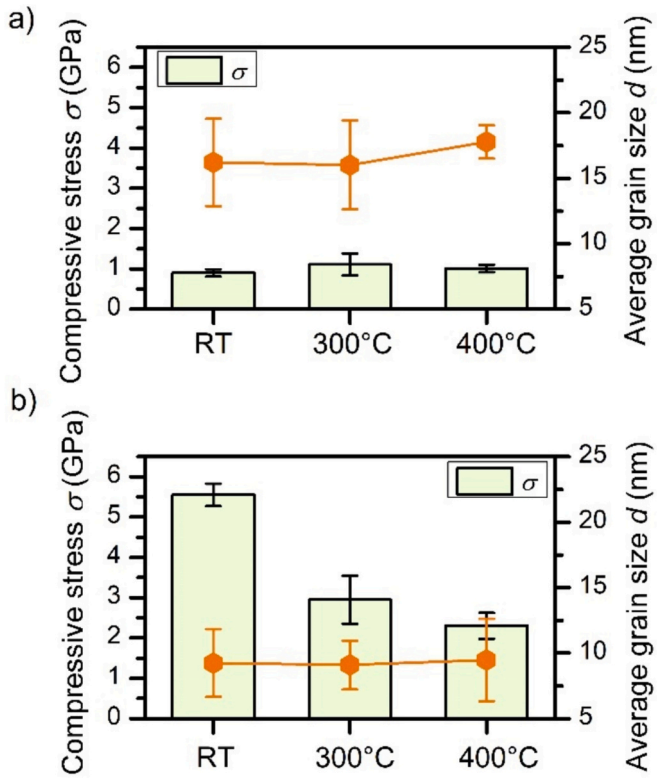

Fig. 11. Average residual stress, σ, and average crystallite size, d, of TiAlN coatings prepared by rotating cylindrical LDMS at various substrate temperatures and at a) a floating potential, and b) at a substrate bias of about −100 V.

relationship between the toughness and residual stress can be declared linear, i.e., coatings with higher compressive stress possess higher nanoindentation toughness. Such dependence compares well with our expectations as the compressive stress is known to hinder (or at least reduce) crack initiation and propagation, and thus, to enhance the toughness. In addition, factors like grain refinement (shown in Fig. 11b) resulting in more complicated grain boundaries, and densification (Fig. 9d–f) also contribute to an increase in energy consumed by allowing crack propagation, and thus, to an enhanced toughness [73]. Similar relationship between residual stress and toughness presented here, has been also reported by other authors, e.g. for TiN coatings [74] or CrAlN coatings [75].

On the other hand, it should be pointed out that the levels of compressive stress to enhance coatings toughness need to be optimized, since excessive residual stresses can be detrimental, causing micro-cracks in the coating, poor adhesion or even delamination.

The toughness values determined here from indentation experiments are in the range between 1.1 MPa·m$^{1/2}$ (σ = −0.9 GPa) up to 5.1 MPa·m$^{1/2}$ (σ = −5.6 GPa). For comparison, K_c values reported in the literature for TiAlN coatings are around 1.1 MPa·m$^{1/2}$ (in [76,77] based on nanoindentation tests) or 2.5 to 4 MPa·m$^{1/2}$ (in [78,79] determined by bending tests).

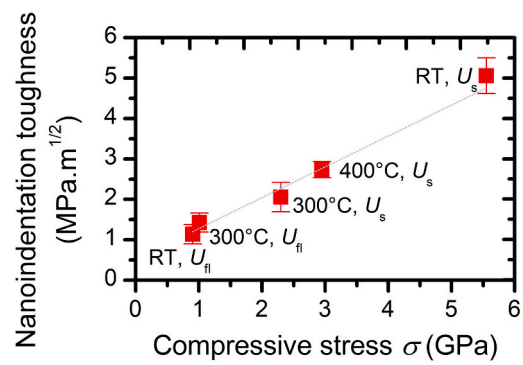

Fig. 13. Nanoindentation toughness of TiAlN coatings prepared by rotating cylindrical LDMS at various substrate temperatures and bias conditions as a function of residual stress.

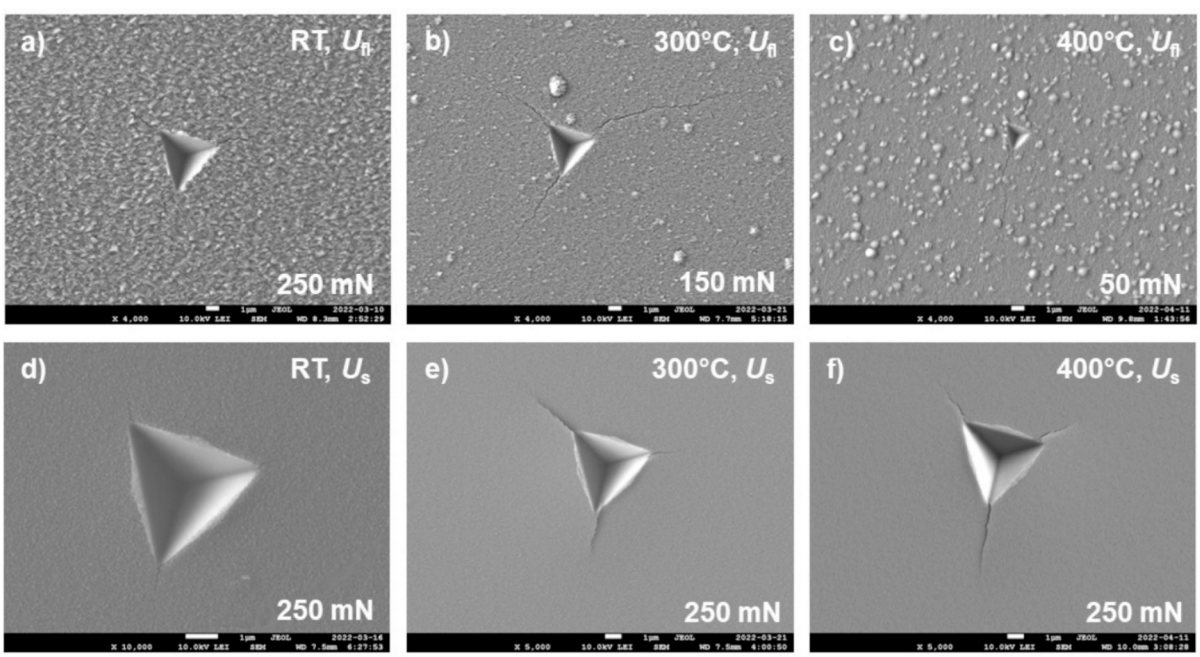

Fig. 12. SEM images of cube-corner pyramidal indents demonstrating crack propagation for the TiAlN coatings prepared by rotating cylindrical LDMS at various substrate temperatures and at a floating potential (a, b, c) and while using substrate bias (d, e, f).

4. Conclusions

In the present work, we assess the use of cylindrical magnetron sputtering (CMS) in low duty cycle pulsed dc magnetron sputtering (LDMS) mode, equipped with a power supply providing a positive kick, for the fabrication of hard TiAlN coatings. We show that the deposition rate in the CMS system in the LDMS mode is only 15 % lower than in the conventional pulsed dc mode, but it is significantly higher (>8×) than HiPIMS deposition using planar magnetrons at comparable power density (in our previous work [40]).

We then investigate the impact of substrate heating and biasing on the composition, microstructure and properties of the TiAlN coatings, with a particular emphasis on the residual stress and the nanoindentation toughness, as critical factors influencing the performance of protective coatings. It is shown that both substrate bias and substrate heating can be effectively used to tune the elasto-plastic properties, residual stress and roughness of the coatings and to optimize them based on the specific application. Using a substrate bias of about −100 V provides TiAlN coatings with a dense compact morphology, high hardness (28–30 GPa), fine crystallite size (~9 nm) and a smooth surface for all substrate temperatures (from room up to 400 °C). Furthermore, the level of compressive stress in the coatings can be selectively reduced by nearly 60 % by increasing substrate temperature from −5.6 GPa to −2.3 GPa at room temperature and 400 °C, respectively.

Based on detailed micromechanical measurements, we found a linear relationship between the residual stress in the TiAlN coatings and their nanoindentation toughness (ranging from 1.1 MPa·m$^{1/2}$ to 5.1 MPa·m$^{1/2}$), which describes the ability of a material to resist crack growth, and thus, is considered to be one of the most important parameters influencing tribological and erosion performance. This creates a solid basis for future investigations of the effect of growth conditions on the stress depth profiles and their optimization for advanced coating architectures that would mitigate the loading stress in different situations.

In summary, the obtained results confirm that CMS is an attractive technique for both optical and protective coating applications. When run in the LDMS mode, this approach offers new opportunities to optimize the process and enhance coating performance. We demonstrate that a high deposition rate can be achieved to produce high-quality protective coatings with tunable properties. TiAlN coatings produced with substrate bias exhibit high hardness, increased compressive stress, as well as H/E_r and H^3/E^2 ratios, which are shown to be indicators of an enhanced toughness. Moreover, substrate heating can be used to significantly reduce the compressive stress in the coatings, which also strongly affects their nanoindentation toughness.

The performance of the optimized TiAlN coatings, including scratch end erosion resistance will be further investigated in conjunction with various advanced coating architectures, and the results will be published in a separate paper.

CRediT authorship contribution statement

Veronika Simova: Writing – review & editing, Writing – original draft, Validation, Methodology, Investigation, Conceptualization. **Oleg Zabeida:** Writing – review & editing, Supervision, Conceptualization. **Luis Bernardo Varela:** Writing – review & editing, Validation, Investigation. **Jincheng Qian:** Validation, Investigation. **Jolanta-Ewa Klemberg-Sapieha:** Writing – review & editing, Resources, Project administration, Conceptualization. **Ludvik Martinu:** Writing – review & editing, Resources, Project administration, Conceptualization.

Declaration of competing interest

The authors declare that they have no known competing financial interests or personal relationships that could have appeared to influence the work reported in this paper.

Acknowledgements

The authors thank Mr. Francis Turcot and Mr. Francis Boutet for their expert technical assistance. We also wish to thank Pedro Avila for his help with lattice parameter calculations. The project has been financially supported by the Natural Sciences and Engineering Research Council of Canada (NSERC) through the grant CRDPJ 520968-17, by Prima Québec (project number R17-13-011), MDS Coating Technologies Corporation, and by IHI Hauzer Techno Coating. We particularly acknowledge the following companies who made available the key equipment for this work, namely Sputtering Components Inc. and robeko GmbH & Co. KG (the rotatable cylindrical magnetron), Magpuls Stromversorgungs Systeme GmbH (the pulse generator), and PLASUS GmbH (the OES system).

Data availability

Data will be made available on request.

References

[1] E. Alfonso, J. Olaya, G. Cubillos, Thin film growth through sputtering technique and its applications, in: Crystallization - Science and Technology, InTech, 2012, pp. 397–432, https://doi.org/10.5772/35844.
[2] A. Behera, S. Aich, T. Theivasanthi, Magnetron sputtering for development of nanostructured materials, in: Design, Fabrication, and Characterization of Multifunctional Nanomaterials, Elsevier, 2021, pp. 177–199, https://doi.org/10.1016/B978-0-12-820558-7.00002-9.
[3] B. Window, Recent advances in sputter deposition, Surf. Coat. Technol. 71 (1995) 93–97, https://doi.org/10.1016/0257-8972(95)80024-7.
[4] G. Bräuer, B. Szyszka, M. Vergöhl, R. Bandorf, Magnetron sputtering – milestones of 30 years, Vacuum 84 (2010) 1354–1359, https://doi.org/10.1016/j.vacuum.2009.12.014.
[5] R. De Gryse, J. Haemers, W.P. Leroy, D. Depla, Thirty years of rotatable magnetrons, Thin Solid Films 520 (2012) 5833–5845, https://doi.org/10.1016/j.tsf.2012.04.065.
[6] N.D. Madsen, B.H. Christensen, S. Louring, A.N. Berthelsen, K.P. Almtoft, L. P. Nielsen, J. Bøttiger, Controlling the deposition rate during target erosion in reactive pulsed DC magnetron sputter deposition of alumina, Surf. Coat. Technol. 206 (2012) 4850–4854, https://doi.org/10.1016/j.surfcoat.2012.05.070.
[7] M. Rudolph, N. Brenning, H. Hajihoseini, M.A. Raadu, J. Fischer, J. T. Gudmundsson, D. Lundin, Operating modes and target erosion in high power impulse magnetron sputtering, J. Vac. Sci. Technol. A 40 (2022) 043005, https://doi.org/10.1116/6.0001919.
[8] J. Čapek, M. Hála, O. Zabeida, J.E. Klemberg-Sapieha, L. Martinu, Steady state discharge optimization in high-power impulse magnetron sputtering through the control of the magnetic field, J. Appl. Phys. 111 (2012) 023301, https://doi.org/10.1063/1.3673871.
[9] I. Safi, Recent aspects concerning DC reactive magnetron sputtering of thin films: a review, Surf. Coat. Technol. 127 (2000) 203–219, https://doi.org/10.1016/S0257-8972(00)00566-1.
[10] A. Blondeel, H. Delrue, S. Matthews, J. Van Holsbeke, W. De Bosscher, Advantages of using rotating cylindrical ito targets for large area coating applications, in: 49th Annual Technical Conference Proceedings of the Society of Vacuum Coaters, 2006, pp. 187–191.
[11] A. Blondeel, P. Persoone, W. De Bosselier, Rotatable magnetron sputter technology for large area glass and web coating, Vak. Forschung Und Prax. 21 (2009) 6–13, https://doi.org/10.1002/vipr.200900384.
[12] S.J. Nadel, P. Greene, J. Rietzel, J. Strümpfel, Equipment, materials and processes: a review of high rate sputtering technology for glass coating, Thin Solid Films 442 (2003) 11–14, https://doi.org/10.1016/S0040-6090(03)00930-1.
[13] A. Blondeel, W. De Bosscher, B. Advanced Coatings, Arc handling in reactive DC magnetron sputter deposition, in: 44th Annual Technical Conference Proceedings of the Society of Vacuum Coaters, 2001, pp. 240–245.
[14] S. Matthews, W. De Bosscher, A. Blondeel, J. Van Holsbeke, H. Delrue, New target materials for innovative applications on glass, Vacuum 83 (2008) 518–521, https://doi.org/10.1016/j.vacuum.2008.04.065.
[15] M. Fahland, O. Zywitzki, T. Modes, K. Vondkar, T. Werner, C. Ottermann, M. Berendt, G. Pollack, Roll-to-roll sputtering of indium tin oxide layers onto ultrathin flexible glass, Thin Solid Films 669 (2019) 56–59, https://doi.org/10.1016/j.tsf.2018.10.032.
[16] J. Rezek, J. Szelwicka, J. Vlček, R. Čerstvý, J. Houška, M. Fahland, J. Fahlteich, Transfer of the sputter technique for deposition of strongly thermochromic VO_2-based coatings on ultrathin flexible glass to large-scale roll-to-roll device, Surf. Coat. Technol. 442 (2022) 128273, https://doi.org/10.1016/j.surfcoat.2022.128273.
[17] X.Y. Li, D. Depla, W.P. Leroy, J. Haemers, R. De Gryse, Influence of deposition on the reactive sputter behaviour during rotating cylindrical magnetron sputtering, J. Phys. D. Appl. Phys. 41 (2008) 025203, https://doi.org/10.1088/0022-3727/41/3/035203.

[18] D. Depla, X.Y. Li, S. Mahieu, K. Van Aeken, W.P. Leroy, J. Haemers, R. De Gryse, A. Bogaerts, Rotating cylindrical magnetron sputtering: simulation of the reactive process, J. Appl. Phys. 107 (2010) 113307, https://doi.org/10.1063/1.3415550.

[19] K. Bobzin, N. Bagcivan, P. Immich, S. Bolz, R. Cremer, T. Leyendecker, Mechanical properties and oxidation behaviour of (Al,Cr)N and (Al,Cr,Si)N coatings for cutting tools deposited by HPPMS, Thin Solid Films 517 (2008) 1251–1256, https://doi.org/10.1016/j.tsf.2008.06.050.

[20] T. Shimizu, H. Komiya, T. Watanabe, Y. Teranishi, H. Nagasaka, K. Morikawa, M. Yang, HIPIMS deposition of TiAlN films on inner wall of micro-dies and its applicability in micro-sheet metal forming, Surf. Coat. Technol. 250 (2014) 44–51, https://doi.org/10.1016/j.surfcoat.2014.02.008.

[21] D. Xie, L.J. Wei, H.Y. Liu, K. Zhang, Y.X. Leng, D.T.A. Matthews, R. Ganesan, Y. Y. Su, Deposition of titanium films on complex bowl-shaped workpieces using DCMS and HiPIMS, Surf. Coat. Technol. 442 (2022) 128192, https://doi.org/10.1016/j.surfcoat.2022.128192.

[22] J. Kohout, E. Bousser, T. Schmitt, R. Vernhes, O. Zabeida, J. Klemberg-Sapieha, L. Martinu, Stable reactive deposition of amorphous Al_2O_3 films with low residual stress and enhanced toughness using pulsed dc magnetron sputtering with very low duty cycle, Vacuum 124 (2016) 96–100, https://doi.org/10.1016/j.vacuum.2015.11.017.

[23] J. Kohout, J. Qian, T. Schmitt, R. Vernhes, O. Zabeida, J. Klemberg-Sapieha, L. Martinu, Hard AlN films prepared by low duty cycle magnetron sputtering and by other deposition techniques, J. Vac. Sci. Technol. A: Vac. Surf. Films 35 (2017), https://doi.org/10.1116/1.4999460.

[24] S. PalDey, S.C. Deevi, Single layer and multilayer wear resistant coatings of (Ti,Al)N: a review, Mater. Sci. Eng. A 342 (2003) 58–79, https://doi.org/10.1016/S0921-5093(02)00259-9.

[25] D. McIntyre, J.E. Greene, G. Håkansson, J.-E. Sundgren, W.-D. Münz, Oxidation of metastable single-phase polycrystalline $Ti_{0.5}Al_{0.5}N$ films: kinetics and mechanisms, J. Appl. Phys. 67 (1990) 1542–1553, https://doi.org/10.1063/1.345664.

[26] L. Chen, J. Paulitsch, Y. Du, P.H. Mayrhofer, Thermal stability and oxidation resistance of Ti-Al-N coatings, Surf. Coat. Technol. 206 (2012) 2954–2960, https://doi.org/10.1016/j.surfcoat.2011.12.028.

[27] N. Norrby, M.P. Johansson-Jõesaar, M. Odén, Improved metal cutting performance with bias-modulated textured $Ti_{0.50}Al_{0.50}N$ multilayers, Surf. Coat. Technol. 257 (2014) 102–107, https://doi.org/10.1016/j.surfcoat.2014.05.045.

[28] G. Greczynski, J. Lu, J. Jensen, S. Bolz, W. Kölker, C. Schiffers, O. Lemmer, J. E. Greene, L. Hultman, A review of metal-ion-flux-controlled growth of metastable TiAlN by HIPIMS/DCMS co-sputtering, Surf. Coat. Technol. 257 (2014) 15–25, https://doi.org/10.1016/j.surfcoat.2014.01.055.

[29] V. Simova, S. Knittel, M. Cavarroc, L. Martinu, J.E. Klemberg-Sapieha, Amorphous Si–B–C–N coatings for high-temperature oxidation protection of the γ-TiAl alloy, Surf. Coat. Technol. 442 (2022), https://doi.org/10.1016/j.surfcoat.2022.128544.

[30] W. Oliver, G. Pharr, An improved technique for determining hardness and elastic modulus using load and displacement sensing indentation experiments, J. Mater. Res. 7 (1992) 1564–1583, https://doi.org/10.1557/JMR.1992.1564.

[31] B.R. Lawn, A.G. Evans, D.B. Marshall, Elastic/plastic indentation damage in ceramics: the median/radial crack system, J. Am. Ceram. Soc. 63 (1980) 574–581, https://doi.org/10.1111/j.1151-2916.1980.tb10768.x.

[32] N. Cuadrado, D. Casellas, M. Anglada, E. Jiménez-Piqué, Evaluation of fracture toughness of small volumes by means of cube-corner nanoindentation, Scr. Mater. 66 (2012) 670–673, https://doi.org/10.1016/j.scriptamat.2012.01.033.

[33] L.B. Varela, P.R.T. Avila, A. Miletić, E. Bousser, J.M. Mendez, J.E. Klemberg-Sapieha, L. Martinu, Residual stress depth profiles self-developed in cathodic arc deposited Ti-Al-N coatings prepared at different constant substrate bias values, J. Vac. Sci. Technol. A 42 (2024) 043104, https://doi.org/10.1116/6.0003555.

[34] T. Gnäupel-Herold, A.A. Creuziger, M. Iadicola, A model for calculating diffraction elastic constants, J. Appl. Crystallogr. 45 (2012) 197–206, https://doi.org/10.1107/S0021889812002221.

[35] J.W. Bradley, H. Backer, P.J. Kelly, R.D. Arnell, Time-resolved Langmuir probe measurements at the substrate position in a pulsed mid-frequency DC magnetron plasma, Surf. Coat. Technol. 135 (2001) 221–228, https://doi.org/10.1016/S0257-8972(00)00990-7.

[36] M. Rahamathunnisa, D.C. Cameron, Ion fluxes in medium frequency pulsed DC magnetron sputtering, Surf. Coat. Technol. 204 (2010) 3131–3134, https://doi.org/10.1016/j.surfcoat.2010.02.055.

[37] V. Šímová, J. Vlček, Š. Zuzjaková, J. Houška, Y. Shen, J. Jiang, E.I. Meletis, V. Peřina, Magnetron sputtered Hf–B–Si–C–N films with controlled electrical conductivity and optical transparency, and with ultrahigh oxidation resistance, Thin Solid Films 653 (2018) 333–340, https://doi.org/10.1016/j.tsf.2018.03.064.

[38] A. Anders, Discharge physics of high power impulse magnetron sputtering, Surf. Coat. Technol. 205 (2011) S1–S9, https://doi.org/10.1016/j.surfcoat.2011.03.081.

[39] J.T. Gudmundsson, D. Lundin, N. Brenning, M.A. Raadu, C. Huo, T.M. Minea, An ionization region model of the reactive Ar/O_2 high power impulse magnetron sputtering discharge, Plasma Sources Sci. Technol. 25 (2016), https://doi.org/10.1088/0963-0252/25/6/065004.

[40] P.R.T. Avila, O. Zabeida, L.B. Varela, J.E. Klemberg-Sapieha, L. Martinu, In-situ monitoring of stress evolution in high power impulse magnetron sputtering-deposited Ti-Al-N films: effect of substrate bias and temperature, Thin Solid Films 784 (2023) 140069, https://doi.org/10.1016/j.tsf.2023.140069.

[41] H. Elmkhah, T.F. Zhang, A. Abdollah-zadeh, K.H. Kim, F. Mahboubi, Surface characteristics for the Ti-Al-N coatings deposited by high power impulse magnetron sputtering technique at the different bias voltages, J. Alloys Compd. 688 (2016) 820–827, https://doi.org/10.1016/j.jallcom.2016.07.013.

[42] L. Zauner, P. Ertelthaler, T. Wojcik, H. Bolvardi, S. Kolozsvári, P.H. Mayrhofer, H. Riedl, Reactive HiPIMS deposition of Ti-Al-N: influence of the deposition parameters on the cubic to hexagonal phase transition, Surf. Coat. Technol. 382 (2020), https://doi.org/10.1016/j.surfcoat.2019.125007.

[43] J. Weichart, M. Lechthaler, Titanium aluminum nitride sputtered by HIPIMS, IOP Conf. Ser. Mater. Sci. Eng. 39 (2012), https://doi.org/10.1088/1757-899X/39/1/012001.

[44] Simple Sputter Yield Calculator, Technische Universität Wien, Institut Für Angewandte Physik. https://www.iap.tuwien.ac.at/www/surface/sputteryield.

[45] M.W. Chase, Nist-janaf Thermochemical Tables, 4th edition, American Institute of Physics, 1998.

[46] M. Rausch, M. Golizadeh, P. Kreiml, M.J. Cordill, J. Winkler, C. Mitterer, Sputter deposition of NiW films from a rotatable target, Appl. Surf. Sci. 511 (2020) 145616, https://doi.org/10.1016/j.apsusc.2020.145616.

[47] H. Rueß, Baben M. to, S. Mráz, L. Shang, P. Polcik, S. Kolozsvári, M. Hans, D. Primetzhofer, J.M. Schneider, HPPMS deposition from composite targets: effect of two orders of magnitude target power density changes on the composition of sputtered Cr-Al-C thin films, Vacuum 145 (2017) 285–289, https://doi.org/10.1016/j.vacuum.2017.08.048.

[48] B.F. Coll, R. Fontana, A. Gates, P. Sathrum, (Ti,Al)N advanced films prepared by arc process, Mater. Sci. Eng. A 140 (1991) 816–824, https://doi.org/10.1016/0921-5093(91)90519-S.

[49] G.P. Zhang, G.J. Gao, X.Q. Wang, G.H. Lv, L. Zhou, H. Chen, H. Pang, S.Z. Yang, Influence of pulsed substrate bias on the structure and properties of Ti-Al-N films deposited by cathodic vacuum arc, Appl. Surf. Sci. 258 (2012) 7274–7279, https://doi.org/10.1016/j.apsusc.2012.03.100.

[50] S.K. Wu, H.C. Lin, P.L. Liu, An investigation of unbalanced-magnetron sputtered TiAlN films on SKH51 high-speed steel, Surf. Coat. Technol. 124 (2000) 97–103, https://doi.org/10.1016/S0257-8972(99)00636-2.

[51] J.E. Greene, J.E. Sundgren, L. Hultman, I. Petrov, D.B. Bergstrom, Development of preferred orientation in polycrystalline TiN layers grown by ultrahigh vacuum reactive magnetron sputtering, Appl. Phys. Lett. 67 (1995) 2928, https://doi.org/10.1063/1.114845.

[52] F. Adibi, I. Petrov, J.E. Greene, L. Hultman, J.-E. Sundgren, Effects of high-flux low-energy (20–100 eV) ion irradiation during deposition on the microstructure and preferred orientation of $Ti_{0.5}Al_{0.5}N$ alloys grown by ultra-high-vacuum reactive magnetron sputtering, J. Appl. Phys. 73 (1993) 8580, https://doi.org/10.1063/1.353388.

[53] W.J. Shen, M.H. Tsai, Y.S. Chang, J.W. Yeh, Effects of substrate bias on the structure and mechanical properties of $(Al_{1.5}CrNb_{0.5}Si_{0.5}Ti)N_x$ coatings, Thin Solid Films 520 (2012) 6183–6188, https://doi.org/10.1016/j.tsf.2012.06.002.

[54] L. Hultman, J.-E. Sundgren, J.E. Greene, Formation of polyhedral N_2 bubbles during reactive sputter deposition of epitaxial TiN (100) films, J. Appl. Phys. 66 (1989) 536–544, https://doi.org/10.1063/1.343570.

[55] D. Gall, S. Kodambaka, M.A. Wall, I. Petrov, J.E. Greene, Pathways of atomistic processes on TiN(001) and (111) surfaces during film growth: an ab initio study, J. Appl. Phys. 93 (11) (2003) 9086–9094, https://doi.org/10.1063/1.1567797.

[56] L. Hultman, J.-E. Sundgren, J.E. Greene, High-flux low-energy (≈20 eV) N_2^+ ion irradiation during TiN deposition by reactive magnetron sputtering: effects on microstructure and preferred orientation, J. Appl. Phys. 78 (1995) 5395, https://doi.org/10.1063/1.359720.

[57] D. Rafaja, C. Wüstefeld, C. Baehtz, V. Klemm, M. Dopita, M. Motylenko, C. Michotte, M. Kathrein, Effect of internal interfaces on hardness and thermal stability of nanocrystalline $Ti_{0.5}Al_{0.5}N$ coatings, Metall. Mater. Trans. A Phys. Metall. Mater. Sci. 42 (2011) 559–569, https://doi.org/10.1007/s11661-010-0204-8.

[58] C. Wüstefeld, D. Rafaja, V. Klemm, C. Michotte, M. Kathrein, Effect of the aluminium content and the bias voltage on the microstructure formation in $Ti_{1-x}Al_xN$ protective coatings grown by cathodic arc evaporation, Surf. Coat. Technol. 205 (2010) 1345–1349, https://doi.org/10.1016/j.surfcoat.2010.07.057.

[59] J.M. Andersson, J. Vetter, J. Müller, J. Sjölén, Structural effects of energy input during growth of $Ti_{1-x}Al_xN$ ($0.55 \leq x \leq 0.66$) coatings by cathodic arc evaporation, Surf. Coat. Technol. 240 (2014) 211–220, https://doi.org/10.1016/j.surfcoat.2013.12.018.

[60] F. Aliaj, N. Syla, S. Avdiaj, T. Dilo, Effect of bias voltage on microstructure and mechanical properties of arc evaporated (Ti, Al)N hard coatings, Bull. Mater. Sci. 36 (2013) 429–435, https://doi.org/10.1007/s12034-013-0479-7.

[61] K.-H. Muller, Ion-beam-induced epitaxial vapor-phase growth: a molecular-dynamics study, Phys. Rev. B 35 (1987) 7906–7913, https://doi.org/10.1103/PhysRevB.35.7906.

[62] M. Naoe, S. Ono, T. Hirata, Crystal orientation in titanium thin films deposited by the sputtering method without plasma damage, Mater. Sci. Eng. A 134 (1991) 1292–1295, https://doi.org/10.1016/0921-5093(91)90976-T.

[63] T. Zhou, P. Nie, X. Cai, P.K. Chu, Influence of N_2 partial pressure on mechanical properties of (Ti,Al)N films deposited by reactive magnetron sputtering, Vacuum 83 (2009) 1057–1059, https://doi.org/10.1016/j.vacuum.2009.01.001.

[64] E.O. Hall, The deformation and ageing of mild steel: III discussion of results, Proc. Phys. Soc. B 64 (1951) 747–753, https://doi.org/10.1088/0370-1301/64/9/303.

[65] N.J. Petch, The cleavage strength of polycrystals, J. Iron Steel Inst. 174 (1953) 25–28.

[66] J.G. Swadener, B. Taljat, G.M. Pharr, Measurement of residual stress by load and depth sensing indentation with spherical indenters, J. Mater. Res. 16 (2001) 2091–2102, https://doi.org/10.1557/JMR.2001.0286.

[67] V. Valvoda, R. Kužel, R. Černý, J. Musil, Structure of TiN coatings deposited at relatively high rates and low temperatures by magnetron sputtering, Thin Solid Films 156 (1988) 53–64, https://doi.org/10.1016/0040-6090(88)90282-9.

[68] S. Hassani, M. Bielawski, W. Beres, L. Martinu, M. Balazinski, J.E. Klemberg-Sapieha, Predictive tools for the design of erosion resistant coatings, Surf. Coat. Technol. 203 (2008) 204–210, https://doi.org/10.1016/j.surfcoat.2008.08.050.
[69] J. Musil, M. Jirout, Toughness of hard nanostructured ceramic thin films, Surf. Coat. Technol. 201 (2007) 5148–5152, https://doi.org/10.1016/j.surfcoat.2006.07.020.
[70] A. Leyland, A. Matthews, On the significance of the H/E ratio in wear control: a nanocomposite coating approach to optimised tribological behaviour, Wear 246 (2000) 1–11, https://doi.org/10.1016/S0043-1648(00)00488-9.
[71] G. Håkansson, J.-E. Sundgren, D. McIntyre, J.E. Greene, W.-D. Münz, Microstructure and physical properties of polycrystalline metastable $Ti_{0.5}Al_{0.5}N$ alloys grown by d.c. magnetron sputter deposition, Thin Solid Films 153 (1987) 55–65, https://doi.org/10.1016/0040-6090(87)90169-6.
[72] J.W. Lee, S.K. Tien, Y.C. Kuo, The effects of pulse frequency and substrate bias to the mechanical properties of CrN coatings deposited by pulsed DC magnetron sputtering, Thin Solid Films 494 (2006) 161–167, https://doi.org/10.1016/j.tsf.2005.07.190.
[73] S. Zhang, D. Sun, Y. Fu, H. Du, Toughening of hard nanostructural thin films: a critical review, Surf. Coat. Technol. 198 (2005) 2–8, https://doi.org/10.1016/j.surfcoat.2004.10.020.
[74] L. Zhang, H. Yang, X. Pang, K. Gao, A.A. Volinsky, Microstructure, residual stress, and fracture of sputtered TiN films, Surf. Coat. Technol. 224 (2013) 120–125, https://doi.org/10.1016/j.surfcoat.2013.03.009.
[75] Y.X. Wang, S. Zhang, J.W. Lee, W.S. Lew, B. Li, Influence of bias voltage on the hardness and toughness of CrAlN coatings via magnetron sputtering, Surf. Coat. Technol. 206 (2012) 5103–5107, https://doi.org/10.1016/j.surfcoat.2012.06.041.
[76] Z.T. Jiang, M.K. Lei, Structure and fracture toughness of TiAlN thin films deposited by deep oscillation magnetron sputtering, Thin Solid Films 754 (2022) 139306, https://doi.org/10.1016/j.tsf.2022.139306.
[77] J.K. Park, C. Ziebert, M. Stüber, Y.J. Baik, Improvement of hardness and toughness of TiAlN coating by nanoscale multilayered structurization with Si_3N_4, Plasma Process. Polym. 4 (2007) S902–S905, https://doi.org/10.1002/ppap.200732202.
[78] G. Jaeger, I. Endler, M. Heilmaier, K. Bartsch, A. Leonhardt, A new method of determining strength and fracture toughness of thin hard coatings, Thin Solid Films 377–378 (2000) 382–388, https://doi.org/10.1016/S0040-6090(00)01312-2.
[79] M. Bartosik, C. Rumeau, R. Hahn, Z.L. Zhang, P.H. Mayrhofer, Fracture toughness and structural evolution in the TiAlN system upon annealing, Sci. Rep. 7 (2017), https://doi.org/10.1038/s41598-017-16751-1.